CHAPTER

7

Soil moisture monitoring using unmanned aerial system

Ruodan Zhuang[1], *Salvatore Manfreda*[2], *Yijian Zeng*[3], *Zhongbo Su*[3,4], *Eyal Ben Dor*[5,6] *and George P. Petropoulos*[7]

[1]Department of European and Mediterranean Cultures: Architecture, Environment, Cultural Heritage, University of Basilicata, Matera, Italy [2]Department of Civil, Building and Environmental Engineering, University of Napoli Federico II, Naples, Italy [3]Faculty of Geo-Information Science and Earth Observation, University of Twente, Enschede, the Netherlands [4]Key Laboratory of Subsurface Hydrology and Ecological Effect in Arid Region of Ministry of Education, School of Water and Environment, Chang'an University, Xi'an, P. R. China [5]Department of Geography and Human Environment, Tel Aviv University, Tel Aviv, Israel [6]Porter School of Environment and Earth Sciences, Faculty of Exact Science, Tel Aviv University, Tel Aviv, Israel [7]Department of Geography, Harokopio University of Athens, Athens, Greece

7.1 Introduction

Soil moisture (SM), the water content of the soil, is a vital element in the hydrological cycle and vegetation growth. Quantification of SM and its spatiotemporal variability are valuable for understanding water availability in agriculture, land–atmosphere interactions, ecosystem states, river basin hydrology, and water resources management (Baldwin et al., 2017; Deng et al., 2019; Manfreda et al., 2014; Peng et al., 2017; Petropoulos et al., 2018; Seneviratne et al., 2004, 2010; Su et al., 2011). SM data can be obtained through multiple sources, including in situ measurements and remote sensing, with different spatial-temporal coverage and resolution. Monitoring SM from unmanned aerial system (UAS) can complement information from ground-based and satellite-based sensors, with relatively higher spatial-resolution and larger spatial coverage at almost any time.

Traditionally, SM can be directly obtained with in situ techniques such as simple gravimetric sampling, various sensors (time-domain reflectometry, amplitude-domain reflectometry, and

frequency-domain reflectometry), which is accurate but usually at the point scale, and highly burdensome. However, SM is a highly heterogeneous variable that may need continuous spatial scale monitoring. To solve this problem, using relatively dense sensor networks is an effective solution to detect the space-time variations of SM not only in the horizontal plane but also along with the vertical profile. Nevertheless, remote sensing can serve as an alternative approach, which provides SM data over various spatiotemporal coverage with high efficiency (Brocca et al., 2017; Colliander et al., 2017; Kerr et al., 2012a,b; Su et al., 2020).

The remote sensing data are used to retrieve SM, including microwave (MW), thermal infrared (TIR) and optical data, over various spatiotemporal coverages. The basic idea behind surface SM data retrieval from remotely sensed information is that the variation of SM can be reflected by the corresponding electromagnetic response of the land surface (Schanda, 2012). For example, the methods to retrieve surface SM from MW remote sensing data are based on the relationship between the dielectric property of soils and SM. Methods utilizing information from optical or TIR remote sensing to retrieve surface SM are based on the relationship between surface SM and surface reflectance (Gao et al., 2013; Nocita et al., 2013). Also, the methods that combine the optical and TIR data (Taktikou et al., 2016; Verstraeten et al., 2006) are based on the thermal characteristics of the soil.

First, passive-MW remote sensing shows a good penetration capability to satisfy various weather and land surface conditions. Several well-established global surface SM products are provided at a relatively coarse resolution (25−36 km) with varying durations, such as the Soil Moisture Active Passive (Entekhabi et al., 2010), the Soil Moisture and Ocean Salinity (Kerr et al., 2012a,b), the Advanced MW Scanning Radiometer for Earth Observing System. Then, active-MW remote sensing can provide higher resolution (10−100 m) images of backscatter signals, but the performance of active-MW remote sensing can be limited by surface roughness or dense vegetation coverage. Several surface SM products based on active-MW remote sensing are available, such as Sentinel-1 C-SAR surface SM product (1-km resolution) over pan-Europe region (Bauer-Marschallinger et al., 2019) and the global surface SM from the Advanced Scatterometer (25-km resolution) (Wagner et al., 2013). In general, passive- and active-MW remote sensing of SM are promising techniques in terms of continuous availability of large-scale data products. However, the available SM data from MW remote sensing are at relatively coarse resolution, which is suitable for large-scale (global or regional) SM study instead of field-scale high-resolution SM research.

However, remote sensing (RS) from satellite does resolve the problem spatial coverage, while the passage of the satellite might generate spatial-temporal issues. Thus SM data merging and climate reanalysis provide a possibility to comprehensively use SM data from multiple sources (Zeng et al., 2016; Zhuang et al., 2020), for instance, the European Space Agency Climate Change Initiative SM product of 25 km (Dorigo et al., 2015) and the European Centre for Medium-Range Weather Forecasts reanalysis (ERA-Interim) data set of 25 km (Balsamo et al., 2015). Nevertheless, one of the important prerequisites of data merging and reanalysis is high-quality SM retrieved from remotely sensed signals.

Furthermore, thermal and optical remote sensing also provide a possibility to observe land surface information at a wide range of resolutions because the thermal and optical signals from the land surface are strong, and the sensors can be mounted not only on satellites but also on crewed airplanes or UASs. For example, the products from the Moderate Resolution Imaging Spectroradiometer (1 km) (Wan, 2014; Wan et al., 2015) and

LANDSAT program (30–100 m optical and TIR data) (Irons et al., 2012; Jimenez-Munoz et al., 2014). However, thermal and optical remote sensing is limited significantly by the weather condition. Nevertheless, airborne remote sensing, especially the UAS, provides a possibility to obtain submeter land surface information efficiently, flexibly, and economically. In various application cases, high-resolution continuous SM maps are necessary. The study usually focuses on a field scale for agricultural applications and requires detailed SM information up to plot/plant scales. Also, drought monitoring and fine-scale water budget assessment are requiring high-resolution SM data.

Numerous studies proved the ability of SM retrieval from UAS-based optical and thermal remote sensing, as SM is known to impact soil reflectance at all wavelengths of the solar spectrum. For spectral-based methods, the Kubelka–Munk (KM) model provides a possibility to derive surface SM directly from shortwave reflectance data (Sadeghi et al., 2015; Yuan et al., 2019), and the physically based models, such as the multilayer radiative transfer model of soil reflectance (MARMIT) (Bablet et al., 2018; Dupiau et al., 2022), are recommended due to the simplicity and the reliability, as long as the prior calibration condition is satisfied. For empirical methods, one of the well-established methods is the thermal inertia method, which was a classical method of satellite-based remote sensing and is currently also applied with UAS data. Paruta et al. (2020) presented an example of using UAS-based thermal inertia method for surface SM estimation over bare soil and sparsely vegetated area and showed a satisfactory result against in situ measured SM data. Another recommended method is the temperature–vegetation triangle method, which makes the evapotranspiration and SM estimation possible. Wang et al. (2018) gave an example of root-zone SM estimation using a modified temperature–vegetation triangle model with the help of land surface roughness data from UAS optical data. Petropoulos et al. (2021) also gave examples of surface SM and evapotranspiration estimation using simplified triangle models and presented high-accuracy results validated with in situ measurements. Also, UAS-based land surface information can be used in the surface SM downscaling procedure with machine learning (ML) (Su et al., 2020; Zhang et al., 2021).

As it is still a primary stage of research on UAS-based SM monitoring, the standardization of operational procedures can be beneficial to understanding and guaranteeing the quality of retrieved SM (Manfreda et al., 2018; Tmušić et al., 2020). For example, when different SM retrieval models are going to be used, the sensor type and the acquisition time should be well-planned based on the theory and the follow-up processing methodology. Thus this chapter aims at providing operational guidance on various approaches for UAS-based SM monitoring to facilitate the follow-up applications.

7.2 Theoretical background of soil moisture retrieval and downscaling methods

This section introduces the theoretical background of five models [i.e., thermal inertia model, two physically based models KM model and MRAMIT, temperature–vegetation triangle model, random forest (RF) regression model]. The last model is an additional recommendation for downscale coarse resolution data, while others link remotely sensed signals with SM. The detailed processing procedures of each method will be introduced in Section 7.4.

7.2.1 Thermal inertia model

Thermal inertia is related to the capacity of heat storage and the thermal conductivity of the soil layer and to the density of the object, which vary depending on SM (Maltese et al., 2013; Pratt et al., 1980). The thermal inertia can influence the heat energy propagation and storage process, thus, link the daily land surface temperature (LST) change to surface SM. The first thermal inertia model was proposed by Watson et al. (1971) with the help of the available TIR data. Then, Price (1977) proved the possibility to generate thermal inertia using remotely sensed data with a generalized theory and proposed the apparent thermal inertia (ATI) model-based on the diurnal surface temperature change over bare soil pixels (Price, 1985; Scheidt et al., 2011). Furthermore, several advanced thermal inertia–based methods were proposed, such as Xue and Cracknell (1995) introduced the real-time model for the thermal inertia estimation. Zhang et al. (2003) considered sensible and latent heat fluxes, and Liu and Zhao (2006) included a two-layer model into the thermal conductivity equation. To map surface SM using remotely sensed optical and TIR data, Minacapilli et al. (2012) evaluated the thermal inertia model with a laboratory experiment and proved the great potential of the model. After several applications of the thermal inertia method over bare soil areas (Kang et al., 2017; Maltese et al., 2010), Paruta et al. (2020) provided a possibility to extend the application of the thermal inertia method over sparse vegetated and shadowed areas, with the help of the high-resolution UAS data and geostatistical analysis. The assumption behind the spatial interpolation of the ATI values is that, given the spatial variability of the SM, the interpolated thermal inertia mimics the value it should assume in the absence of vegetation (and/or shadows) if caused only by SM. This assumption was experimentally verified in the research (Paruta et al., 2020).

The soil thermal inertia of a specific material reveals the speed of characteristic thermal change respond to the energy flux exchange, which can be expressed as the following function (Maltese et al., 2010):

$$P = \sqrt{\lambda \rho C} \tag{7.1}$$

where P is the thermal inertia ($J/m^2/K\ (s)^{1/2}$), λ is thermal conductivity (W/m/K), ρ is the density of the material, C is the specific heat for unit mass. Suppose the specific material is a layer of soil containing an amount of soil water content. In that case, the relationship between thermal inertia P and SM can be linked by λ and C. In short, SM positively correlates with λ and C. To derive P from remotely sensed optical and TIR data, the solving of thermal diffusion differential equations was executed under various hypotheses (Maltese et al., 2010; Pratt and Ellyett, 1979). A simplified form of thermal inertia, ATI (K^{-1}) was proved well and linearly correlated with SM (Minacapilli et al., 2012). The theory of ATI accounts for the daily LST variation and the albedo, which can be easily determined using optical and TIR data of the two extreme temperature-time points. ATI can be expressed as the following equation:

$$\mathrm{ATI} = (1 - \alpha)/\Delta T \tag{7.2}$$

where ΔT is the maximum daily LST difference, α is the surface albedo. The ΔT can be easily determined using the LST maps obtained from the highest and lowest temperature

time point, and α can be determined using optical data [visible and near-infrared (VIS-NIR) reflectance data, usually from the multispectral camera]. The simple of the linear relationship between SM and ATI can be expressed as follows:

$$\theta = a * ATI + b \tag{7.3}$$

where a and b are empirical parameters, which can be determined with the help of ground truth data (Chang et al., 2012; Minacapilli et al., 2012; Qin et al., 2013; Sobrino and El Kharraz, 1999; Xue and Cracknell, 1995).

7.2.2 Kubelka–Munk model and multilayer radiative transfer model of soil reflectance

The KM model is a simple model to retrieve surface SM from optical remotely sensed data, which was developed based on the KM theory (Kubelka and Munk, 1931). The parameters in the KM model are physically definable. The basic idea of the KM theory can be illustrated in Fig. 7.1. The gray rectangle space represents an absorbing and scattering layer, and the KM theory can describe the radiative transfer in the layer; I and J are a downward and an upward light propagation flux, which are perpendicular to the layer. The KM model can be derived under several assumptions: (1) the layer is infinite; (2) uniformly distributed light absorbing and scattering; (3) particle dimensions are much smaller when compared with the depth of the layer; (4) an illumination homogeneous layer (Ciani et al., 2005). The differential equations describing radiance I and J can be expressed as the following equation:

$$dI(\lambda, z)/dz = -(k+s)I(\lambda, z) + sJ(\lambda, z) \tag{7.4}$$

$$dJ(\lambda, z)/dz = -(k+s)J(\lambda, z) - sI(\lambda, z) \tag{7.5}$$

where the units of I and J are ($W/m^2/sr$), z (m) is the depth of the layer, λ is the wavelength. k (m^{-1}) is the light absorption coefficient, and s (m^{-1}) is the light scattering coefficient.

Then, the reflectance (R) and transmittance can be derived by analytically solving the equations (transmittance tends to zero when the depth of the layer keeps increasing).

$$R = 1 + k/s - \sqrt{(k/s)^2 + 2k/s} \tag{7.6}$$

$$r = k/s = (1-R)^2/2R \tag{7.7}$$

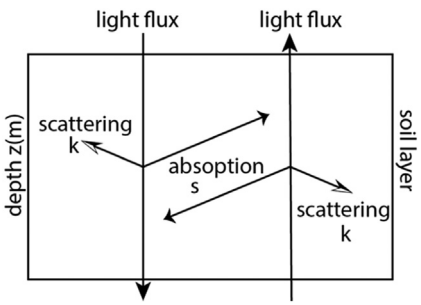

FIGURE 7.1 Visualization of KM theory (Kubelka and Munk, 1931). *KM*, Kubelka–Munk.

Then, apply the KM theory to a thick soil layer, k and s are functions of soil particle characteristics and soil water content. Assuming that k and s can be treated as an additive function of their constituents with a weight of their proportion (Barron and Torrent, 1986; Ciani et al., 2005; Hu and Johnston, 2009). The k and s can be expressed as follows:

$$k = k_{solid}(1-\theta_s) + k_{water}\theta + k_{air}(\theta_s - \theta) \tag{7.8}$$

$$s = s_{solid}(1-\theta_s) + s_{water}\theta + s_{air}(\theta_s - \theta) \tag{7.9}$$

where θ is the volumetric water content, and θs is the volumetric water content under the saturated status. And when the coefficients of air are negligible, the functions can be simplified as:

$$k = k_d + k_{water}\theta \tag{7.10}$$

$$s = s_d + s_{water}\theta \tag{7.11}$$

To sum up, the yield function is:

$$r = (1-R)^2/2R = (k_d + k_{water}\theta)/(s_d + s_{water}\theta) \tag{7.12}$$

The absorption and scattering coefficients of dry or wet soil samples can be measured in the lab. As the ratio of k/s related directly to the reflectance, the function can be rearranged as follows:

$$r = \left(\sigma r_d\left(1-\theta/\theta_s\right) + r_s\left(\theta/\theta_s\right)\right)/\left(\sigma\left(1-\theta/\theta_s\right) + \left(\theta/\theta_s\right)\right) \tag{7.13}$$

$$r_d = k_d/s_d = (1-R_d)^2/2R_d \tag{7.14}$$

$$r_s = k_s/s_s = (1-R_s)^2/2R_s \tag{7.15}$$

$$\sigma = s_d/s_s = s_d/(s_d + s_{water}\theta_s) \tag{7.16}$$

The parameter r of dry and saturated soil can be determined directly from remotely sensed reflectance data. The parameter σ provides a metric in dry and saturated soils for the relative strength of scattering. Thus, to derive surface SM from remote sensed optical data, the function can be:

$$\theta/\theta_s = \sigma(r - r_d)/(r_s - r + \sigma(r - r_d)) \tag{7.17}$$

If the scattering of soil water is negligible compared to that of dry soil, the parameter σ approaches unity. In some appropriate wavelengths such as short-wavelength infrared (SWIR), model conditions may be met as they are strong water-absorbing bands (e.g., 2500, 1950, and 1450 nm wavelength). Then a simple function of surface SM retrieval is established:

$$\theta/\theta_s = (r - r_d)/(r_s - r_d) \tag{7.18}$$

Therefore surface SM can be simply retrieved from remotely sensed reflectance data using the abovementioned functions.

Another alternative physically based model is the MRAMIT, which is a radiative transfer model which assume the wet soil as a water layer overlay on the dry soil layer (Ångström, 1925; Lekner and Dorf, 1988). The MRAMIT 1 is improved from the Bach model (Bach and Mauser, 1994), which account for light absorption in the water layer

using the Beer–Lambert–Bouguer law, and the MRAMIT 2 is an improved version of the MARMIT 1, both of them predicting the spectral reflectance of wet soils in the solar domain (Bablet et al., 2018; Dupiau et al., 2022).

Compare with the KM model, MRAMIT models have a wider range of application when refers to the spectrum range (the KM model is applicable in the water-absorbing bands, while MRAMIT models is suitable over the entire solar spectrum).

7.2.3 Simplified temperature–vegetation triangle model

The temperature–vegetation triangle, which was first proposed by Price (1990), is based on the inherent relationship between LST and evapotranspiration. Thus the remotely sensed LST and vegetation fraction could be used to estimate SM from surface to root zone. The triangle space can be created using the scatter plots of vegetation fraction and LST, including various soil wet conditions (from dry end to wet end) and vegetation coverage conditions (from bare soil to densely vegetated conditions). A simplified temperature–vegetation triangle was proposed by Carlson and Petropoulos (2019) and recently validated using UAS data (Petropoulos et al., 2021) and using sentinel-3 satellite data (Petropoulos et al., 2020). As presented in Fig. 7.2, the scaled LST (T^*)—vegetation fraction (Fr) triangle feature space consists of an upper decreasing boundary of dry edge, and two mutually perpendicular boundaries indicate full ranges of soil water condition and vegetation coverage. It is a simple and efficient method without the requirement of ground truth data.

Three assumptions were made to apply the temperature–vegetation model. First, the atmospheric forcing should be homogeneous, which is easy to satisfy in the UAS application case as the areas covered by UAS surveys are generally small. Second, over similar vegetation coverage, the surface roughness should be homogeneous. Third, the image used for

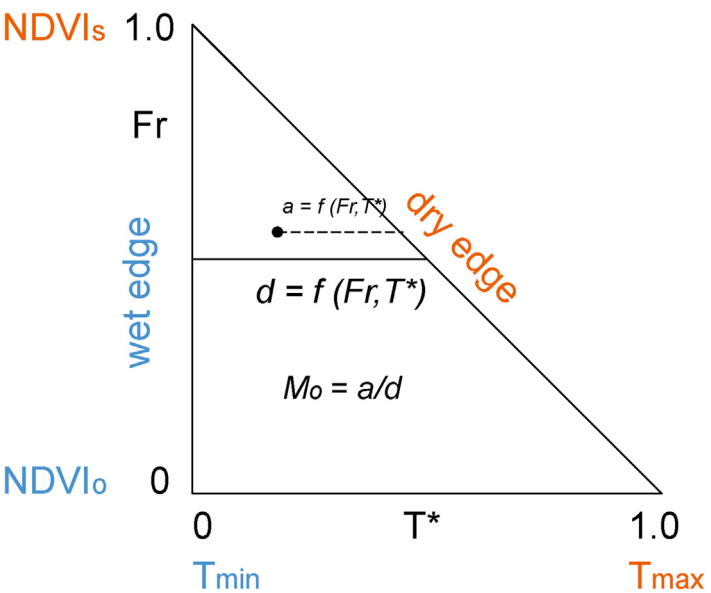

FIGURE 7.2 Conceptualization of the main properties encapsulated in a Ts/VI scatter plot (Petropoulos et al., 2009).

establishing the triangle space should be large enough to cover wet and dry edges of different surface conditions, that is, needs a wide range of variability in vegetation cover present in the area. The last two assumptions are somehow challenging to satisfy in the UAS-based data due to the limited coverage of UAS mapping and the canopy height dynamic under natural conditions. Wang et al. (2018) proposed to use the digital surface model based on the structure-from-motion (SfM) technique to correct the roughness and introduce a theoretical dry and wet edge calculated from in situ measurements, if available.

7.2.4 Random forest regression model

A possible strategy to map high-resolution SM can also be the downscaling strategy that links coarse SM with related high-resolution variables. Remarkably, SM heterogeneity in time and space makes this task very challenging. As a function of input data and characteristics of models, different downscaling methods have been proposed (for a recent review, please see Peng et al. (2017)), such as physical model−based method, data assimilation method, and statistical regression method.

Among them, empirical methods are known for the conciseness of theory and practicality, as they provide a possibility to facilitate the understanding of the highly nonlinear relationship between surface SM and land surface features (Atkinson, 2013; Camps-Valls et al., 2018). In this context, ML methods train algorithms with enough data to get a comprehensive environmental response function for surface SM estimation, regardless of the complex physical characteristics (Cai et al., 2019; Cui et al., 2020; Holtgrave et al., 2018; Liu et al., 2017). ML algorithms used for downscaling include artificial neural network (ANN), support vector machines (SVM), RF, among others. ANN is widely used as a universal approximator that performs well in pedotransfer function predictions (Zhang et al., 2018), while SVM has been proved to have the ability to solve regression problems and used in high-resolution surface SM estimation (Araya et al., 2020; Yan and Bai, 2020). Finally, most ML methods have been used as a black box (Amoore, 2019), while RF regression models also provide the possibility to evaluate the importance of each predictor. However, the limitation of the ML methods is the high requirement of the amount of data for model training when compare with the other SM retrieval methods. Thus, except for the data from the UAS survey, a large amount of related information from different sources should be prepared beforehand.

The RF Method, proposed by Breiman (2001), is a popularly used ML method, which can be applied in classification, regression, and other tasks. For regression tasks, some decision trees are first built during the training time, and the mean prediction of the individual trees is generated as the output of this method. In general, according to the adaptive nature of the decision rules involved in it, RF has the advantage in modeling the complex nonlinear relationships between the predictors and the response variable instead of detailed numerical expressions (Hutengs and Vohland, 2016). In detail, the input data act as the training data in the RF method, and RF divides them into many regression trees, making up the forest, where each tree is built from a bootstrap sample, which contains about two-thirds of the input data. Each split is selected from a random subset of a given number (m) of the p variables. During this process, the number of trees (n_{tree}) is also a key parameter in the forest. For each bootstrap sampling process, the left samples will not be

included in the model construction, and they act as the out-of-bag samples or OOB, which is an important feature of RF. The OOB can be used to validate the performance of the constructed model, and the mean squared error based on OOB samples is a reliable test error estimate, which is almost identical to that obtained by K-fold cross-validation.

7.3 Data acquisition and preprocessing

7.3.1 Unmanned aerial system flights and data acquisition

The general protocols for UAS-based observation can be referred to contents described in Chapter 3. For SM monitoring the target is acquiring high-quality VIS (wavelength of 0.750−0.40 μm), NIR (wavelength of 2.5−0.75 μm), and TIR (wavelength of 25−2.5 μm) data, which refers to the UAS surveys with an RGB (red, green and blue bands) camera, multispectral camera, and thermometers. A fixed-flight survey with stable flight speed via double-gridded routes is necessary to obtain good quality images, especially thermal images.

The UAS surveys with multispectral cameras aim to collect vegetation cover information and albedo. Thus the acquisition time is usually at the mid-day for the minimum shadow area with a clear clouds condition. The UAS surveys with a thermometer aim to obtain the LST. The important information in the thermal inertia method is the maximum land surface difference, indicating soil thermal characteristics. As such, two surveys, one at the time point of sunrise and one at the mid-day, are planned to represent the highest and lowest LST. The UAS survey with an RGB camera aims to produce a digital surface model to generate the topographic information, which can be conducted at any time with a clear view of the field.

7.3.2 Data preprocessing

A comprehensive description of processing the USA data can be found in Chapter 12. The contents in this chapter are focused on the preprocessing of data related to SM monitoring, which mainly refers to the radiometric calibration of TIR and optical sensors and the resultant LST map and the multispectral reflectance maps. Other procedures like flight mission planning, camera setting can be referred to in Chapter 3, and the orthomosaic procedure based on the SfM can be referred to in Chapter 4.

The radiometric calibration of sensors is necessary to obtain precise data, as the UAS sensors usually have low signal-to-noise ratios (Berni et al., 2009; Laliberte et al., 2011). The accuracy of thermal sensors could be influenced by the target temperature and the temperature of the camera itself. A climate-controlled laboratory calibration with a black body radiation source can be performed to obtain accurate thermal images and link the digital number (DN) with the target temperature. Also, a simultaneously in situ measured temperature of the targets, which appears in the remotely sensed thermal images, with TIR cameras can serve as a radiometric calibration and atmospheric correction. The corrected thermal image can well represent the LST of the acquisition time after a field calibration using aluminum paper covered targets as references.

For the multispectral sensor, reflectance calibration and radiometric calibration are also necessary. Similarly, the simultaneously in situ spectroradiometric measurements of black

and white panels are required to construct the relationship between the calibrated reflectance values of each wavelength and DN values in each band of the multispectral images. Once the quality of the calibrated reflectance maps of red, green, and NIR bands is guaranteed, normalized difference vegetation index (NDVI) and the shortwave albedo map can be generated simply using band calculation. One point to be noted for albedo calculation, the weights of summation can be determined considering the normalized relative spectral response (RSR, the short-circuit current density generated by unit of irradiance at a particular wavelength as a function of wavelength).

7.4 Soil moisture data retrieval and downscaling

7.4.1 Surface soil moisture retrieval using thermal inertia method

For surface SM retrieval using the thermal inertia method, LST maps and multispectral reflectance maps from the data preprocessing can be used. If the spatial resolution and coverage of LST maps and reflectance maps are different, an alignment is required for further processing. The flowchart of the processing procedure can be found in Fig. 7.3.

First, albedo can be calculated using the reflectance of red, green, and NIR bands by weighted summation. A convolution between the RSR of multispectral sensors and solar irradiance can be used to determine the weights of the sensor of the UAS survey. Furthermore, the multispectral reflectance maps can also be used to simply calculate the NDVI map, which can be used to mask out shadowed and vegetated pixels of the LST maps by empirical threshold values. However, other classification methods, such as the RF classification, can also be an option to distinguish shadowed and vegetated pixels, which is not satisfied by the application condition of the thermal inertia method.

Then, a series of simple calculations of masked maps should be executed, including the LST difference (ΔT) map calculation from two LST maps and the ATI maps calculation with the function mentioned above-using albedo and ΔT maps. To obtain the empirical relationship (the regression model) between surface SM and ATI, several in situ measured surface SM data can be used as a reference. With the empirical relationship and the prepared ATI map, the surface SM map over bare soil pixels can be easily calculated. The example map of ATI and SM can be found in Fig. 7.3. However, two points of the classical procedure deserve to be discussed. First, the performance of the empirical relationship model needs to be tested by comparing the estimated surface SM with the in situ measured data using statistical methods. Second, semivariogram and kriging interpolation may extend the application from bare soil pixels to shadow and sparse vegetated pixels (Paruta et al., 2020). The best spatial resolution can be evaluated by testing gradually changed diameters of buffers around the validation points of surface SM.

7.4.2 Surface soil moisture retrieval using the Kubelka–Munk model

The application of the KM model requires the remotely sensed reflectance data from appropriate SWIR bands. From the preprocessing data phase, the optical band's reflectance maps (vegetated pixels are flagged out with help of the NDVI map) are ready to use. The

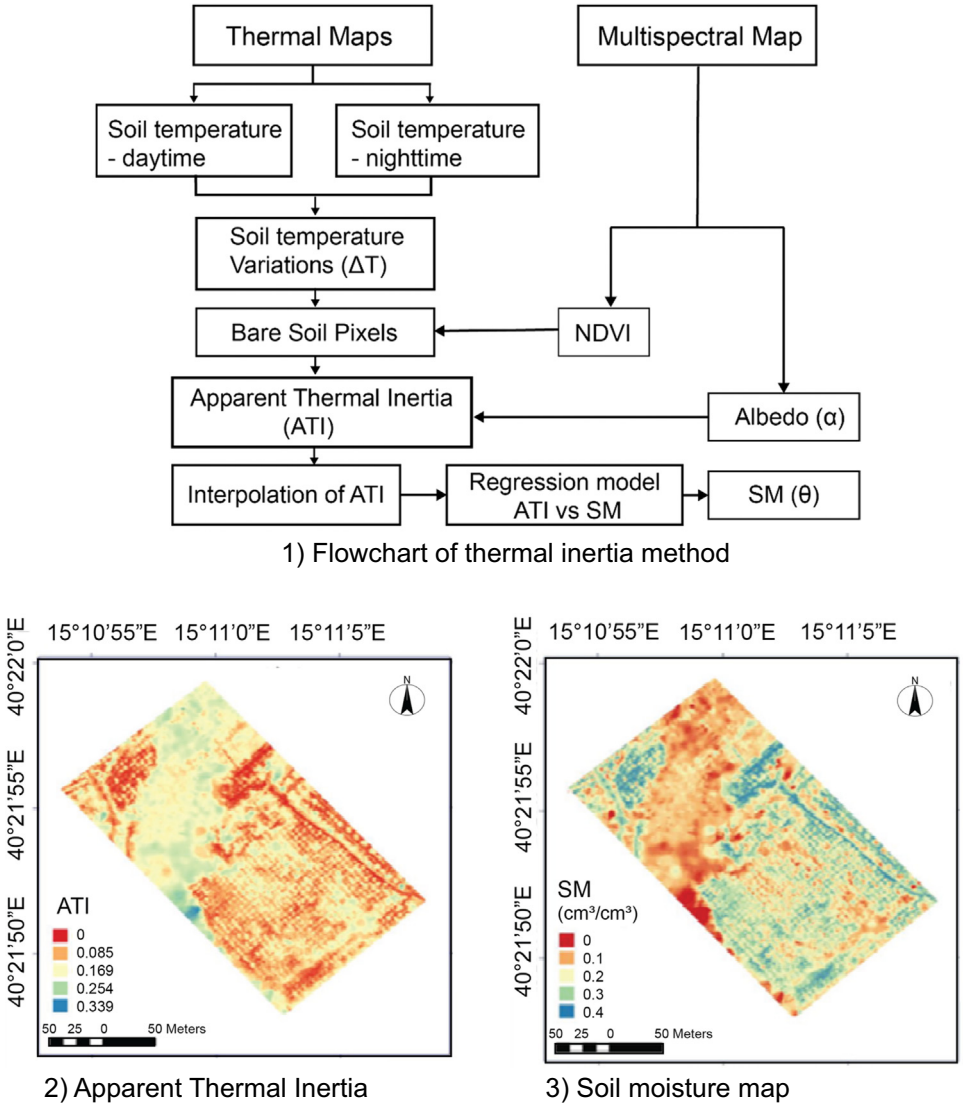

FIGURE 7.3 Methodology of thermal inertia method and example maps of apparent thermal inertia and SM (Paruta et al., 2020). *SM*, Soil moisture.

processing procedure is presented in Fig. 7.4. The first step is calculating r using function (7.12). Then, the reflectance of the dry and saturated conditions can also be found in the reflectance maps, which can be further used to derive r_d and r_s. In the end, with the knowledge of saturated surface SM, the surface SM map can be calculated directly based on the function and the known parameters. The simplicity and the physical basis of the KM model make it a reliable and efficient tool for optical remote sensing-based SM estimation.

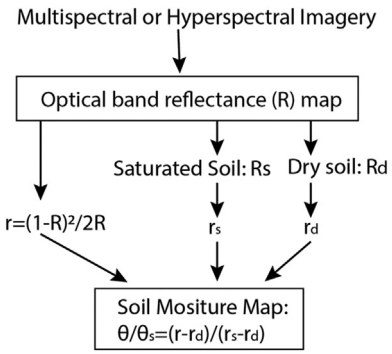

FIGURE 7.4 Flowchart describing the KM model. *KM*, Kubelka–Munk.

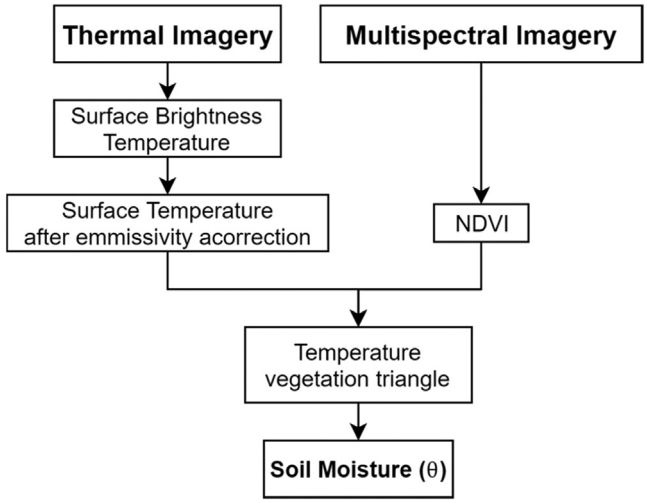

FIGURE 7.5 Methodology flowchart of the simplified temperature–vegetation triangle model.

7.4.3 Soil moisture retrieval using the simplified temperature–vegetation triangle model

The simplified temperature–vegetation triangle model inputs include the LST and NDVI derived from the reflectance values measured by the UAS-borne multispectral camera at red and NIR wavelengths (Fig. 7.5). It is worth noting that the LST for the case of partial vegetative cover conditions means a mixture of bare soil surface temperature and vegetation canopy temperature.

To guarantee the performance of the triangle model, the UAS survey should be executed in a relatively flat area with heterogeneous vegetation coverage (a full range of vegetation fraction values to be present).

The first step to implement the triangle model is identifying some representative pixels, such as the full vegetation-covered pixel and the bare soil pixel. This step can be easily operated by choosing the highest and lowest values of LST and NDVI on the images.

The second step is calculating vegetation fraction based on the NDVI values of each pixel in the map and the NDVI values over full vegetated coverage and bare soil pixels. The function of vegetation fraction calculation (Gillies et al., 1997) can be expressed as follows:

$$Fr = (\mathrm{NDVI} - \mathrm{NDVI}_0)/(\mathrm{NDVI}_S - \mathrm{NDVI}_0) \tag{7.19}$$

where NDVI_o is the NDVI value over the bare soil pixel, and NDVI_s is the NDVI value over the full vegetated pixel.

Then, the scaled LST (also called the temperature dryness index (Sandholt et al., 2002)) can be calculated using the following function:

$$T^* = (T - T_{min})/(T_{max} - T_{min}) \tag{7.20}$$

where T_{min} is the lowest LST value in the image, and T_{max} is the highest LST value in the image. Thus both the vegetation fraction (Fr) and the scaled LST (T^*) range from 0 to 1.

The next step is constructing the two-dimensional triangle space by plotting Fr versus T^* values of each pixel. An example of a scatter plot can be found in Fig. 7.6. Several essential features of the triangle space need to be explained. First, the warm edge (or the dry edge) can be found as the hypotenuse of the triangle, from the vertex of highest Fr and lowest T^* to the vertex of lowest Fr and highest T^*. The physical meaning of the warm edge can be explained as where the maximum temperature occurs in different vegetation coverage categories, and the high temperature refers to a dry condition. Second, the cold

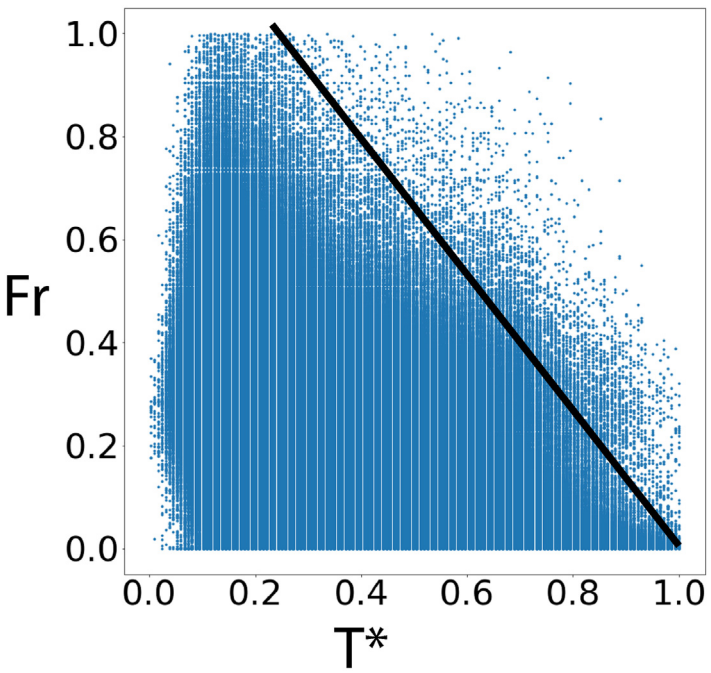

FIGURE 7.6 Scatter plots derived in a test in a cropland in southern Italy, in June 2019.

edge or wet edge is where the minimum T^* appears in each vegetation coverage category, which tends to be vertical in the plot. Wet edge refers to the values of soil water availability, and evapotranspiration equals 1. Then the soil line is the bottom line in the plots, which indicates the bare soil conditions with NDVI, or Fr equals 0. Furthermore, the triangle vertex is possible to be a flattened top like in Fig. 7.6. It can be caused by various reasons, like the highest NDVI values in this region are not representing the full vegetation coverage.

After the construction of the triangle space, the evapotranspiration and soil water availability can be estimated with two hypotheses: first, the transpiration is equal to the potential transpiration when vegetation is at wilting point; second, the relationship between soil water availability and evapotranspiration fraction is linear within the triangle domain. Thus, as presented in Fig. 7.2, soil water availability and evapotranspiration can be defined with the following function:

$$M_o = 1 - T^*(pixel)/T^*(dryedge) \tag{7.21}$$

$$EF = EF_{soil}(1 - Fr) + FrEF_{veg} = M_o(1 - Fr) + Fr \tag{7.22}$$

where M_o is the soil water availability, EF_{soil} is the ratio between soil evaporation and net radiation, and the EF_{veg} equals 1.

7.5 Soil moisture downscaling using random forest regression model

The basic processing procedures are presented in Fig. 7.7.

The predictors used in the RF regression model include various land surface features related to SM, such as rainfall, vegetation index, LST, elevation, topographic information, and soil properties. In the SM downscaling study, the coarse resolution surface SM data are used to train the RF regression model and validate the model results. The detailed processing steps are the following:

1. Synchronize predictors and coarse resolution surface SM datasets in terms of temporal and spatial coverage and resolution. Create as many pairs of predictors of surface SM data as the input of the RF regression model.
2. A part of data pairs (70% were recommended) can be used to train the RF regression model. Then the predictors' data in the other part of the data pairs are used to estimate surface SM using the well-tuned RF regression model. The estimated surface SM (also coarse resolution) can be validated with the original coarse resolution surface SM data.
3. If the validation result (the left 30%) of the previous step is satisfactory, the trained RF regression model can be used in the following steps. Otherwise, either the predictors' combination or the spatial-temporal coverage of the data used for model training should be adjusted to produce reliable results.
4. Using fine resolution predictors data as the input of the trained RF regression model, the output result is the fine resolution surface SM data. Fig. 7.8 is an example located in southern Italy. The RF regression model was established with a 5-year 30-m resolution SM (Fig. 7.8 (1)) land surface features (i.e., surface temperature, vegetation index, and

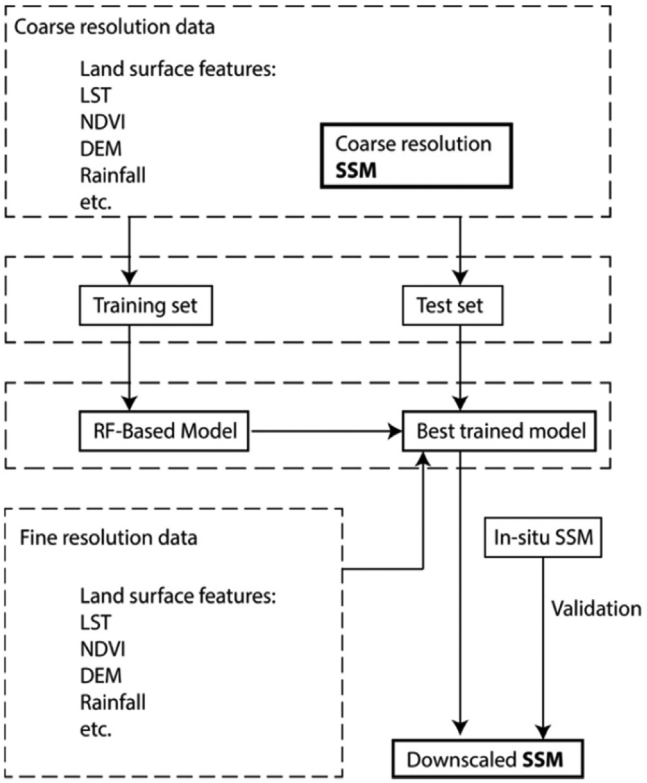

FIGURE 7.7 Methodology of the random forest regression model downscaling (Zhang et al., 2021).

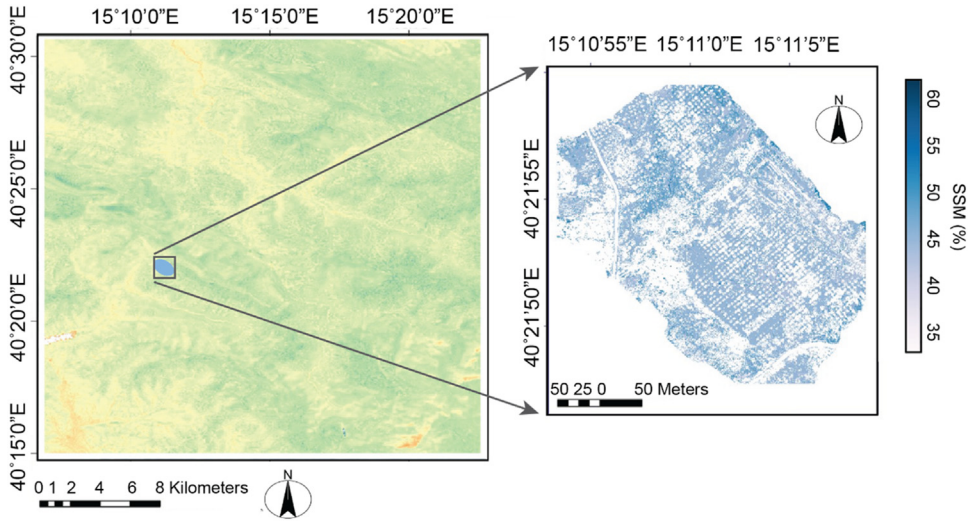

FIGURE 7.8 Example of RF regression downscaling: (1) a 5-year average of downscaled 30-m resolution SM map; and (2) estimated 16-cm resolution SM map on June 13, 2019. *SM*, Soil moisture.

slope), and applied with UAS-based land surface information, the resolution of the result SM is 16 cm (Fig. 7.8 (2)).

To achieve a reasonable and reliable modeling result, the selection of appropriate predictors is worth to be discussed. In the coarse resolution and large-scale case, some specific variables play important roles, such as rainfall, geographic information, and LST. In the fine resolution and small-scale case (e.g., UAS data, submeter resolution, field scale), the vegetation, soil texture, and LST become the most important information. However, it is not possible to isolate their individual effects (Crow et al., 2012), and the combinations of variables can influence the accuracy of the downscaling results. It is important to perform a comprehensive analysis before selecting downscaling predictors (Das et al., 2011; Im et al., 2016; Kathuria et al., 2019; Panciera et al., 2008).

7.6 Discussion and conclusions

In this chapter the importance of SM and the necessity of the high-resolution SM mapping on field-scale studies are introduced. Then, a review on the applications of UAS-based SM monitoring presents the potential of the suggested SM approaches. Providing several alternative models for UAS-based data management, including optical data-based KM model, TIR data−based thermal inertia method and the simplified temperature−vegetation triangle method, and RF regression model−based spatial downscaling strategy, are introduced in detail with their theory and operation procedures, characteristics, and constraining and a summary of each method can be found in Table 7.1.

In general, the thermal inertia method is suitable for bare soil areas and sparsely vegetated areas and very much convenient for UAS utilization as broadband thermal with RGB cameras are usually the basic apparatus system for the most common UAS. Numerous studies have been conducted to guarantee the reliability of this method, and the studies using UAS-based data gave satisfactory results. But it is necessary to acquire some in situ measured SM simultaneous with the UAS flight mission to calibrate the model. In recent studies, Paruta et al. (2020) presented an application over an agriculture area with relatively high accuracy of SM estimation results and a possibility to extend the research to the vegetated and shaded pixels. The simplified temperature−vegetation triangle model is recommended over densely vegetated regions. The most important advantage of this method is the absence of ancillary atmospheric and surface parameters and land surface models. The results of the study by Petropoulos et al. (2021) showed an acceptable error of 0.040 cm^3/cm^3 for surface SM, which implies that the proposed model performs well under the semiarid conditions as in the study area of this research.

The KM model is recommended due to its simplicity and reliability if a hyperspectral sensor is available in the UAS survey. Once well-acquired SWIR reflectance map is available, SM can be retrieved follow the simple methodology as in Fig. 7.4. Yuan et al. (2019) provided a reliable example of SM retrieval using the KM model with the help of satellite-based data and concluded that a high degree of heterogeneity, surface roughness, topographical features, shadow effects could be the challenges of the application of this method. To extend the application of the KM model to UAS-based surveys, the most

TABLE 7.1 Summary of UAS-based soil moisture (SM) monitoring methods.

	Methods	Sensors; acquisition time	Land surface information	Conditions; strength; limitation	Representative studies
SM retrieval	Apparent thermal inertia method	−TIR; sunrise and noon −Optical (red, green, NIR); noon	−LST −NDVI −Albedo	−Surface SM over bare soil and sparsely vegetated areas;−Reliable;−In situ measurements are required	Paruta et al. (2020)
	Kubelka−Munk method	−Optical (SWIR); noon	−Reflectance	−Surface SM; −Simplicity; −Hyperspectral sensor required	Yuan et al. (2019)
	MARMIT	−Optical; noon	−Reflectance	−Surface SM; −Simplicity; −Hyperspectral sensor required	Bablet et al. (2018), Dupiau et al. (2022)
	Simplified temperature −vegetation triangle method	−TIR −Optical (red, NIR); noon	−LST −NDVI	−Surface SM and evapotranspiration over densely and heterogeneous vegetated areas; −Not require any ancillary parameters and land surface model; −UAS-based applications can be developed more	Petropoulos et al. (2021)
Downscaling	Random Forest Regression	−TIR −Optical (red, green, NIR); noon	−LST −NDVI −DSM, etc.	−Surface SM; −Fully use all available data; −Difficult to validate	Zhang et al. (2021)

LST, Land surface temperature; *NDVI*, normalized difference vegetation index; *NIR*, near-infrared; *TIR*, thermal infrared.

challenging task is obtaining the SWIR reflectance map at field scale, which requires a well calibrated hyperspectral camera. However, the UAS survey usually executed at the field scale, which may provide a suitable condition for the model application with a relatively low degree of heterogeneity, and a reliable surface roughness map, and movable shadow effects.

Except for SM retrieval, UAS-based land surface information can also be used to perform surface SM downscaling with the help of ML models, which can take advantage of available satellite-based SM and land surface data. The methodology has been well established in the research of Zhang et al. (2021) in the global scale study and presented a preliminary result using UAS-based data in the study of Su et al. (2020).

For future works the effort to develop the methods mentioned earlier can be focused on: (1) investigating the special condition or assumption over the relatively small scales (field scale, covered by UAS surveys), (2) investigating the possibility to take advantage of hyperresolution data (submeter resolution, possible to distinguish an individual plant), (3) validation of the results high-resolution SM maps, which indicates not only point scale ground truth validation but also the spatial dynamics of SM.

Acknowledgments

We wish to thank the COST Action CA16219 "HARMONIOUS—Harmonization of UAS techniques for agricultural and natural ecosystems monitoring" for coordination of the research activities. We also would like to thank the European Commission and Netherlands Organisation for Scientific Research (NWO) for funding, in the frame of the collaborative international consortium (iAqueduct) financed under the 2018 Joint call of the Water Works 2017 ERA-NET Cofund. This ERA-NET is an integral part of the activities developed by the Water JPI (Project number: ENWWW.2018.5).

References

Amoore, L., 2019. Doubt and the algorithm: on the partial accounts of machine learning. Theory, Cult. Soc. 36, 147–169.

Araya, S.N., Fryjoff-Hung, A., Anderson, A., Viers, J.H., Ghezzehei, T.A., 2020. Advances in soil moisture retrieval from multispectral remote sensing using unmanned aircraft systems and machine learning techniques. Hydrol. Earth Syst. Sci. 25, 2739–2758.

Ångström, A., 1925. The albedo of various surfaces of ground. Geografiska Annaler 7, 323–342.

Atkinson, P.M., 2013. Downscaling in remote sensing. Int. J. Appl. Earth Obs. Geoinf. 22, 106–114.

Bablet, A., Vu, P.V.H., Jacquemoud, S., Viallefont-Robinet, F., Fabre, S., Briottet, X., et al., 2018. MARMIT: a multilayer radiative transfer model of soil reflectance to estimate surface soil moisture content in the solar domain (400–2500 nm). Remote Sens. Environ. 217, 1–17.

Bach, H., Mauser, W., 1994. Modelling and model verification of the spectral reflectance of soils under varying moisture conditions. Int. Geosci. Remote Sens. Symp. 4, 2354–2356.

Baldwin, D., Manfreda, S., Keller, K., Smithwick, E.A.H., 2017. Predicting root zone soil moisture with soil properties and satellite near-surface moisture data across the conterminous United States. J. Hydrol. 546, 393–404.

Balsamo, G., Albergel, C., Beljaars, A., Boussetta, S., Brun, E., Cloke, H., et al., 2015. ERA-Interim/Land: a global land surface reanalysis data set. Hydrol. Earth Syst. Sci. 19, 389–407.

Barron, V., Torrent, J., 1986. Use of the Kubelka-Munk theory to study the influence of iron oxides on soil colour. J. Soil. Sci. 37, 499–510.

Bauer-Marschallinger, B., Freeman, V., Cao, S., Paulik, C., Schaufler, S., Stachl, T., et al., 2019. Toward global soil moisture monitoring with Sentinel-1: harnessing assets and overcoming obstacles. IEEE Trans. Geosci. Remote Sens.: a Publ. IEEE Geosci. Remote Sens. Soc. 57, 520–539.

Berni, J., Zarco-Tejada, P.J., Suarez, L., Fereres, E., 2009. Thermal and narrowband multispectral remote sensing for vegetation monitoring from an unmanned aerial vehicle. IEEE Trans. Geosci. Remote Sens.: a Publ. IEEE Geosci. Remote Sens. Soc. 47, 722–738.

Breiman, L., 2001. Random forests. Mach. Learn. 45, 5–32.

Brocca, L., Crow, W.T., Ciabatta, L., Massari, C., De Rosnay, P., Enenkel, M., et al., 2017. A review of the applications of ASCAT soil moisture products. IEEE J. Sel. Top. Appl. Earth Obs. Remote Sens. 10 (5): 2285–2306.

Cai, Y., Zheng, W., Zhang, X., Zhangzhong, L., Xue, X., 2019. Research on soil moisture prediction model based on deep learning. PLoS One 14, e0214508.

Camps-Valls, G., Martino, L., Svendsen, D.H., Campos-Taberner, M., Muñoz-Marí, J., Laparra, V., et al., 2018. Physics-aware Gaussian processes in remote sensing. Appl. Soft Comput. 68, 69–82.

Carlson, T.N., Petropoulos, G.P., 2019. A new method for estimating of evapotranspiration and surface from optical and thermal infrared measurements: the simplified triangle. Int. J. Remote Sens. 40, 7716–7729.

Chang, T.Y., Wang, Y.C., Feng, C.C., Ziegler, A.D., Giambelluca, T.W., Liou, Y.A., 2012. Estimation of root zone soil moisture using apparent thermal inertia with MODIS imagery over a tropical catchment in Northern Thailand. IEEE J. Sel. Top. Appl. Earth Obs. Remote Sens. 5, 752–761.

Ciani, A., Goss, K.-U., Schwarzenbach, R.P., 2005. Light penetration in soil and particulate minerals. Eur. J. Soil. Sci. 56, 561–574.

Colliander, A., Jackson, T.J., Bindlish, R., Chan, S., Das, N., Kim, S.B., et al., 2017. Validation of SMAP surface soil moisture products with core validation sites. Remote Sens. Environ. 191, 215–231.

Crow, W.T., Berg, A.A., Cosh, M.H., Loew, A., Mohanty, B.P., Panciera, R., et al., 2012. Upscaling sparse ground-based soil moisture observations for the validation of coarse-resolution satellite soil moisture products. Rev. Geophys. 50, 1–20.

Cui, Y., Chen, X., Xiong, W., He, L., Lv, F., Fan, W., et al., 2020. A soil moisture spatial and temporal resolution improving algorithm based on multi-source remote sensing data and GRNN model. Remote Sens. 12, 455.

Das, N.N., Entekhabi, D., Njoku, E.G., 2011. An algorithm for merging SMAP radiometer and radar data for high-resolution soil-moisture retrieval. IEEE Trans. Geosci. Remote Sens.: a Publ. IEEE Geosci. Remote Sens. Soc. 49, 1504–1512.

Deng, K.A.K., Lamine, S., Pavlides, A., Petropoulos, G.P., Bao, Y., Srivastava, P.K., Guan, Y., 2019. Large scale operational soil moisture mapping from passive MW radiometry: SMOS product evaluation in Europe & USA. Int. J. Appl. Earth. Obs. Geoinf. 80, 206–217.

Dorigo, W.A., Gruber, A., De Jeu, R.A.M., Wagner, W., Stacke, T., Loew, A., et al., 2015. Evaluation of the ESA CCI soil moisture product using ground-based observations. Remote Sens. Environ. 162, 380–395.

Dupiau, A., Jacquemoud, S., Briottet, X., Fabre, S., Viallefont-Robinet, F., Philpot, W., et al., 2022. MARMIT-2: an improved version of the MARMIT model to predict soil reflectance as a function of surface water content in the solar domain. Remote Sens. Environ. 272, 112951.

Entekhabi, D., Njoku, E.G., O'Neill, P.E., Kellogg, K.H., Crow, W.T., Edelstein, W.N., et al., 2010. The Soil Moisture Active Passive (SMAP) mission. Proc. IEEE 98, 704–716.

Gao, Z., Xu, X., Wang, J., Yang, H., Huang, W., Feng, H., 2013. A method of estimating soil moisture based on the linear decomposition of mixture pixels. Math. Computer Model. 58, 606–613.

Gillies, R.R., Kustas, W.P., Humes, K.S., 1997. A verification of the "triangle" method for obtaining surface soil water content and energy fluxes from remote measurements of the Normalized Difference Vegetation Index (NDVI) and surface e. Int. J. Remote Sens. 18, 3145–3166.

Holtgrave, A.-K., Förster, M., Greifeneder, F., Notarnicola, C., Kleinschmit, B., 2018. Estimation of soil moisture in vegetation-covered floodplains with Sentinel-1 SAR data using support vector regression. PFG – J. Photogram. Remote Sens. Geoinf. Sci. 86, 85–101.

Hu, X., Johnston, W.M., 2009. Concentration additivity of coefficients for maxillofacial elastomer pigmented to skin colors. Dental Mater.: Off. Publ. Acad. Dental Materials 25, 1468–1473.

Hutengs, C., Vohland, M., 2016. Downscaling land surface temperatures at regional scales with random forest regression. Remote Sens. Environ. 178, 127–141.

Im, J., Park, S., Rhee, J., Baik, J., Choi, M., 2016. Downscaling of AMSR-E soil moisture with MODIS products using machine learning approaches. Environ. Earth Sci. 75, 1120.
Irons, J.R., Dwyer, J.L., Barsi, J.A., 2012. The next Landsat satellite: the Landsat Data Continuity Mission. Remote Sens. Environ. 122, 11–21.
Jimenez-Munoz, J.C., Sobrino, J.A., Skokovic, D., Mattar, C., Cristobal, J., 2014. Land surface temperature retrieval methods from Landsat-8 thermal infrared sensor data. IEEE Geosci. Remote Sens. Lett. 11, 1840–1843.
Kang, J., Jin, R., Li, X., Ma, C., Qin, J., Zhang, Y., 2017. High spatio-temporal resolution mapping of soil moisture by integrating wireless sensor network observations and MODIS apparent thermal inertia in the Babao River Basin, China. Remote Sens. Environ. 191, 232–245.
Kathuria, D., Mohanty, B.P., Katzfuss, M., 2019. A nonstationary geostatistical framework for soil moisture prediction in the presence of surface heterogeneity. Water Resour. Res. 55, 729–753.
Kerr, Y., Waldteufel, P., Wigneron, J.-P., Boutin, J., Reul, N., Al Bitar, A., et al., 2012a. The Soil Moisture and Ocean Salinity (SMOS) Mission: first results and achievements. RFPT 12–19.
Kerr, Y.H., Waldteufel, P., Richaume, P., Wigneron, J.P., Ferrazzoli, P., Mahmoodi, A., et al., 2012b. The SMOS soil moisture retrieval algorithm. IEEE Trans. Geosci. Remote Sens.: a Publ. IEEE Geosci. Remote Sens. Soc. 50, 1384–1403.
Kubelka, P., Munk, F., 1931. An article on optics of paint layers. Z. Tech. Phys. 12, 259–274.
Laliberte, A.S., Goforth, M.A., Steele, C.M., Rango, A., 2011. Multispectral remote sensing from unmanned aircraft: image processing workflows and applications for rangeland environments. Remote Sens. 3, 2529–2551.
Lekner, J., Dorf, M.C., 1988. Why some things are darker when wet. Appl. Opt. 27 (7), 1278–1280. 27, 1278–1280.
Liu, Z., Zhao, Y., 2006. Research on the method for retrieving soil moisture using thermal inertia model. Sci. China Ser. D. Earth Sci 49, 539–545.
Liu, Y., Yang, Y., Jing, W., Yue, X., 2017. Comparison of different machine learning approaches for monthly satellite-based soil moisture downscaling over Northeast China. Remote Sens. 10, 31.
Maltese, A., Minacapilli, M., Cammalleri, C., Ciraolo, G., D'Asaro, F., 2010. A thermal inertia model for soil water content retrieval using thermal and multispectral images. In: Remote Sensing for Agriculture, Ecosystems, and Hydrology XII. Presented at the Remote Sensing for Agriculture, Ecosystems, and Hydrology XII, International Society for Optics and Photonics, pp. 78241G.
Maltese, A., Bates, P.D., Capodici, F., Cannarozzo, M., Ciraolo, G., La Loggia, G., 2013. Critical analysis of thermal inertia approaches for surface soil water content retrieval. Hydrol. Sci. J. 58, 1144–1161.
Manfreda, S., Brocca, L., Moramarco, T., Melone, F., Sheffield, J., 2014. A physically based approach for the estimation of root-zone soil moisture from surface measurements. Hydrol. Earth Syst. Sci. 18, 1199–1212.
Manfreda, S., McCabe, M.F., Miller, P.E., Lucas, R., Pajuelo Madrigal, V., Mallinis, G., et al., 2018. On the use of unmanned aerial systems for environmental monitoring. Remote Sens. 10, 641.
Minacapilli, M., Cammalleri, C., Ciraolo, G., D'Asaro, F., Iovino, M., Maltese, A., 2012. Thermal inertia modeling for soil surface water content estimation: a laboratory experiment. Soil. Sci. Soc. Am. J. 76, 92–100.
Nocita, M., Stevens, A., Noon, C., van Wesemael, B., 2013. Prediction of soil organic carbon for different levels of soil moisture using Vis-NIR spectroscopy. Geoderma 199, 37–42.
Panciera, R., Walker, J.P., Kalma, J.D., Kim, E.J., Hacker, J.M., Merlin, O., et al., 2008. The NAFE'05/CoSMOS Data Set: toward SMOS soil moisture retrieval, downscaling, and assimilation. IEEE Trans. Geosci. Remote Sens. 46 (3), 736–745.
Paruta, A., Ciraolo, G., Capodici, F., Manfreda, S., Sasso, S.F.D., Zhuang, R., et al., 2020. A Geostatistical approach to map near-surface soil moisture through hyperspatial resolution thermal inertia. IEEE Trans. Geosci. Remote Sens.: a Publ. IEEE Geosci. Remote Sens. Soc. 1–18.
Peng, J., Loew, A., Merlin, O., Verhoest, N.E.C., 2017. A review of spatial downscaling of satellite remotely sensed soil moisture: downscale satellite-based soil moisture. Rev. Geophysics (Washington, D.C.: 1985) 55, 341–366.
Petropoulos, G., Carlson, T.N., Wooster, M.J., Islam, S., 2009. A review of Ts/VI remote sensing based methods for the retrieval of land surface energy fluxes and soil surface moisture. Prog. Phys. Geogr.: Earth Environ. 33 (2), 224–250.
Petropoulos, G.P., Srivastava, P.K., Ferentinos, K.P., Hristopoulos, D., 2020. Evaluating the capabilities of optical/TIR imaging sensing systems for quantifying soil water content. Geocarto Int. 35, 494–511.
Petropoulos, G.P., Maltese, A., Carlson, T.N., Provenzano, G., Pavlides, A., Ciraolo, G., et al., 2021. Exploring the use of unmanned aerial vehicles (UAVs) with the simplified "triangle" technique for soil water content and evaporative fraction retrievals in a Mediterranean setting. Int. J. Remote Sens. 42, 1623–1642.

Petropoulos, G.P., Srivastava, P.K., Piles, M., Pearson, S., 2018. Earth observation-based operational estimation of soil moisture and evapotranspiration for agricultural crops in support of sustainable water management. Sustainability (Switzerland) 10 (1), 181.
Pratt, D.A., Ellyett, C.D., 1979. The thermal inertia approach to mapping of soil moisture and geology. Remote Sens. Environ. 8, 151–168.
Pratt, D.A., Foster, S.J., Ellyett, C.D., 1980. A calibration procedure for Fourier series thermal inertia models. Photogramm. Eng. Remote Sens. 46, 529–538.
Price, J.C., 1977. Thermal inertia mapping: a new view of the Earth. J. Geophys. Res. 82, 2582–2590.
Price, J.C., 1985. On the analysis of thermal infrared imagery: the limited utility of apparent thermal inertia. Remote Sens. Environ. 18, 59–73.
Price, J.C., 1990. Using spatial context in satellite data to infer regional scale evapotranspiration. IEEE Trans. Geosci. Remote Sens.: a Publ. IEEE Geosci. Remote Sens. Soc. 28, 940–948.
Qin, J., Yang, K., Lu, N., Chen, Y., Zhao, L., Han, M., 2013. Spatial upscaling of in-situ soil moisture measurements based on MODIS-derived apparent thermal inertia. Remote Sens. Environ. 138, 1–9.
Sadeghi, M., Jones, S.B., Philpot, W.D., 2015. A linear physically-based model for remote sensing of soil moisture using short wave infrared bands. Remote Sens. Environ. 164, 66–76.
Sandholt, I., Rasmussen, K., Andersen, J., 2002. A simple interpretation of the surface temperature/vegetation index space for assessment of surface moisture status. Remote Sens. Environ. 79, 213–224.
Schanda, E., 2012. Physical Fundamentals of Remote Sensing. Springer Science & Business Media.
Scheidt, S., Lancaster, N., Ramsey, M., 2011. Eolian dynamics and sediment mixing in the Gran Desierto, Mexico, determined from thermal infrared spectroscopy and remote-sensing data. Geol. Soc. Am. Bull. 123, 1628–1644.
Seneviratne, S.I., Viterbo, P., Lüthi, D., Schär, C., 2004. Inferring changes in terrestrial water storage using ERA-40 reanalysis data: the Mississippi River Basin. J. Clim. 17, 2039–2057.
Seneviratne, S.I., Corti, T., Davin, E.L., Hirschi, M., Jaeger, E.B., Lehner, I., et al., 2010. Investigating soil moisture–climate interactions in a changing climate: a review. Earth-Sci. Rev. 99, 125–161.
Sobrino, J.A., El Kharraz, M.H., 1999. Combining afternoon and morning NOAA satellites for thermal inertia estimation: 2. Methodology and application. J. Geophys. Res. Atmos. 104, 9455–9465.
Su, Z., Wen, J., Dente, L., Velde, R.V.D., Wang, L., Ma, Y., et al., 2011. The Tibetan Plateau observatory of plateau scale soil moisture and soil temperature (Tibet-Obs) for quantifying uncertainties in coarse resolution satellite and model products. Hydrol. Earth Syst. Sci. 15, 2303–2316.
Su, Z., Zeng, Y., Romano, N., Manfreda, S., Francés, F., Ben Dor, E., et al., 2020. An integrative information aqueduct to close the gaps between satellite observation of water cycle and local sustainable management of water resources. Water 12, 1495.
Taktikou, E., Bourazanis, G., Papaioannou, G., Kerkides, P., 2016. Prediction of soil moisture from remote sensing data. Procedia Eng. 162, 309–316.
Tmušić, G., Manfreda, S., Aasen, H., James, M.R., Gonçalves, G., Ben-Dor, E., et al., 2020. Current practices in UAS-based environmental monitoring. Remote Sens. 12, 1001.
Verstraeten, W.W., Veroustraete, F., van der Sande, C.J., Grootaers, I., Feyen, J., 2006. Soil moisture retrieval using thermal inertia, determined with visible and thermal spaceborne data, validated for European forests. Remote Sens. Environ. 101, 299–314.
Wagner, W., Hahn, S., Kidd, R., Melzer, T., Bartalis, Z., Hasenauer, S., et al., 2013. The ASCAT soil moisture product: a review of its specifications, validation results, and emerging applications. Meteorol. Zeitschrift. 22, 5–33.
Wan, Z., 2014. New refinements and validation of the collection-6 MODIS land-surface temperature/emissivity product. Remote Sens. Environ. 140, 36–45.
Wan, Z., Hook, S., Hulley, G., 2015. MOD11A1 MODIS/Terra land surface temperature/emissivity daily L3 global 1km SIN Grid V006 [WWW Document]. NASA EOSDIS L. Process. DAAC. <https://doi.org/10.5067/MODIS/MOD11A1.006> (accessed 11.23.19).
Wang, S., Garcia, M., Ibrom, A., Jakobsen, J., Köppl, C.J., Mallick, K., et al., 2018. Mapping root-zone soil moisture using a temperature–vegetation triangle approach with an unmanned aerial system: incorporating surface roughness from structure from motion. Remote Sens. 10, 1978.
Watson, K., Rowen, L.C., Offield, T.W., 1971. Application of thermal modeling in the geologic interpretation of IR images. Remote Sens. Environ. 3.

Xue, Y., Cracknell, A.P., 1995. Advanced thermal inertia modelling. Int. J. Remote Sens. 16, 431–446.
Yan, R., Bai, J., 2020. A new approach for soil moisture downscaling in the presence of seasonal difference. Remote Sens. 12, 2818.
Yuan, J., Wang, X., Yan, C.-X., Wang, S.-R., Ju, X.-P., Li, Y., 2019. Soil moisture retrieval model for remote sensing using reflected hyperspectral information. Remote Sens. 11, 366.
Zeng, Y., Su, Z., Van der Velde, R., Wang, L., Xu, K., Wang, X., et al., 2016. Blending satellite observed, model simulated, and in situ measured soil moisture over Tibetan Plateau. Remote Sens. 8, 268.
Zhang, R., Sun, X., Zhu, Z., Su, H., Tang, X., 2003. A remote sensing model for monitoring soil evaporation based on differential thermal inertia and its validation. Sci. China Ser. D. Earth Sci 46, 342–355.
Zhang, H., Kurtz, W., Kollet, S., Vereecken, H., Franssen, H.-J.H., 2018. Comparison of different assimilation methodologies of groundwater levels to improve predictions of root zone soil moisture with an integrated terrestrial system model. Adv. Water Resour. 111, 224–238.
Zhang, L., Zeng, Y., Zhuang, R., Szabó, B., Manfreda, S., Han, Q., et al., 2021. In situ observation-constrained global surface soil moisture using random forest model. Remote Sens. 13, 4893.
Zhuang, R., Zeng, Y., Manfreda, S., Su, Z., 2020. Quantifying long-term land surface and root zone soil moisture over Tibetan Plateau. Remote Sens. 12, 509.